



Kinetic Scale Magnetic Reconnection with a Turbulent Forcing: Particle-in-cell Simulations

San Lu^{1,2,3} , Quanming Lu^{1,2,3} , Rongsheng Wang^{1,2,3} , Xinmin Li^{1,2,3} , Xinliang Gao^{1,2,3} , Kai Huang^{1,2,3} ,
Haomin Sun^{1,2,3} , Yan Yang⁴ , Anton V. Artemyev^{5,6} , Xin An⁵ , and Yingdong Jia⁵ 

¹ Deep Space Exploration Laboratory, School of Earth and Space Sciences, University of Science and Technology of China, Hefei 230026, People's Republic of China; lusan@ustc.edu.cn, qmlu@ustc.edu.cn

² Chinese Academy of Sciences (CAS) Center for Excellence in Comparative Planetology, CAS Key Lab of Geospace Environment Hefei 230026, People's Republic of China

³ Collaborative Innovation Center of Astronautical Science and Technology, Harbin, People's Republic of China

⁴ Department of Physics and Astronomy, University of Delaware, DE 19716, USA

⁵ Department of Earth, Planetary, and Space Sciences, University of California, Los Angeles, CA 90095, USA

⁶ Space Research Institute of the Russian Academy of Sciences, Moscow 117997, Russia

Received 2022 November 23; revised 2022 December 21; accepted 2023 January 1; published 2023 January 31

Abstract

Turbulent magnetic reconnection has been observed by spacecraft to occur commonly in terrestrial magnetosphere and the solar wind, providing a new scenario of kinetic scale magnetic reconnection. Here by imposing a turbulent forcing on ions in particle-in-cell simulations, we simulate kinetic scale turbulent magnetic reconnection. We find formation of fluctuated electric and magnetic fields and filamentary currents in the diffusion region. Reconnection rate does not change much compared to that in laminar Hall reconnection. At the X-line, the electric and magnetic fields both exhibit a double power-law spectrum with a spectral break near local lower-hybrid frequency. The energy conversion rate is high in turbulent reconnection, leading to significant electron acceleration at the X-line. The accelerated electrons form a power-law spectrum in the high energy range, with a power-law index of about 3.7, much harder than one can obtain in laminar reconnection.

Unified Astronomy Thesaurus concepts: [Solar magnetic reconnection \(1504\)](#); [Interplanetary turbulence \(830\)](#); [Solar energetic particles \(1491\)](#)

1. Introduction

Magnetic reconnection is a fundamental plasma process during which magnetic field topologies change and magnetic energy is converted to plasma energy (Yamada et al. 2010). Magnetic reconnection occurs ubiquitously in various plasma environments, such as the solar corona (e.g., Masuda et al. 1994; Tsuneta 1996; Somov & Kosugi 1997; Su et al. 2013), the solar wind (e.g., Gosling et al. 2005; Phan et al. 2006, 2021; Wang et al. 2022), and Earth's magnetosphere (e.g., Øieroset et al. 2001; Burch et al. 2016; Wang et al. 2017; Torbert et al. 2018; Lu et al. 2022a). It is widely believed to be responsible for the energy conversion and dissipation processes in these environments, with scales ranging from large, magnetohydrodynamic (MHD) scales to small, particle kinetic scales.

In large, MHD scales, the classical Sweet–Parker reconnection model (Parker 1957; Sweet 1958) gives a too slow reconnection rate so that it cannot well describe the reconnection process, for example, in the solar corona. Later, Lazarian & Vishniac (1999) found that the presence of a turbulent component of the reconnecting magnetic field can increase the reconnection rate dramatically. Such type of fast magnetic reconnection was thereafter validated by MHD simulations of magnetic reconnection with an external turbulent forcing (e.g., Kowal et al. 2009, 2012; Loureiro et al. 2009; Yang et al. 2020; Sun et al. 2022). Self-generated turbulence via formation of plasmoids was also found to realize fast magnetic reconnection

according to MHD theories and simulations (e.g., Loureiro et al. 2007; Bhattacharjee et al. 2009; Pucci & Velli 2014). Using solar corona images, Cheng et al. (2018) observed turbulent magnetic reconnection in a current sheet during a solar flare, providing direct evidence for the occurrence of MHD turbulent reconnection.

In small, kinetic scales, fast magnetic reconnection is not necessarily turbulent. The laminar Hall reconnection picture derived from numerous spacecraft observations (e.g., Nagai et al. 2001; Borg et al. 2005; Eastwood et al. 2010) and numerical simulations (e.g., Pritchett 2001; Lu et al. 2010) can well describe kinetic scale fast reconnection. Nevertheless, kinetic scale turbulent magnetic reconnection is still common in space, as shown by many in situ spacecraft observations in Earth's magnetosphere (Eastwood et al. 2009; Huang et al. 2012; Osman et al. 2015; Zhou et al. 2021; Ergun et al. 2022; Jin et al. 2022; Li et al. 2022a, 2022b) and the solar wind (Vörös et al. 2014; Wang et al. 2022).

Simulation and observational efforts have been made to understand kinetic scale turbulent magnetic reconnection, and its cause has been attributed to the following instabilities, waves, and coherent structures: Particle-in-cell (PIC) simulations showed that secondary tearing instability can form secondary magnetic islands (or secondary flux ropes) to develop turbulent magnetic reconnection (e.g., Daughton et al. 2011; Lu et al. 2019). Such a scenario, turbulent reconnection consisting of secondary magnetic islands, was observed thereafter by spacecraft in the magnetotail (e.g., Wang et al. 2016; Fu et al. 2017; Lu et al. 2020). PIC simulations found that lower-hybrid drift instability can form turbulences during magnetic reconnection (e.g., Divin et al. 2015a; Price et al. 2016, 2017), which was also confirmed by



Original content from this work may be used under the terms of the [Creative Commons Attribution 4.0 licence](#). Any further distribution of this work must maintain attribution to the author(s) and the title of the work, journal citation and DOI.

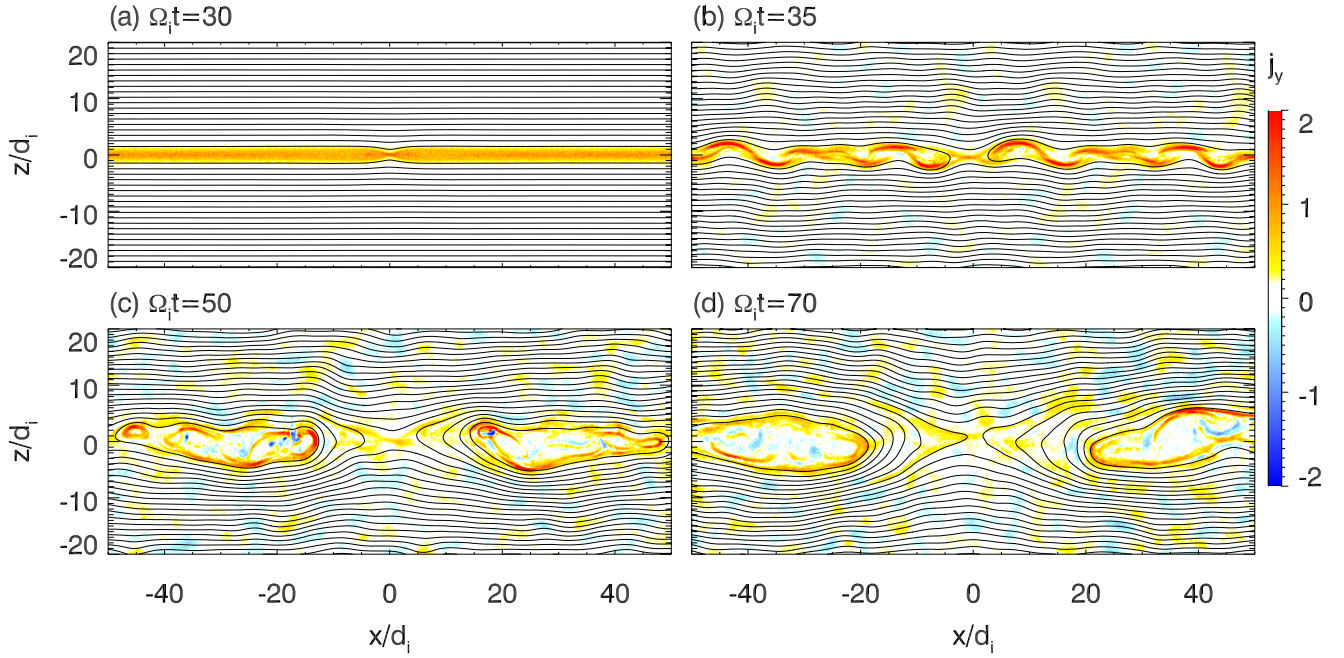


Figure 1. Out-of-plane current density j_y , and in-plane magnetic field lines at $\Omega_i t =$ (a) 30, (b) 35, (c) 50, and (d) 70 in case with a turbulent forcing $dV_0 = 0.03V_A$. The current density is in units of en_0V_A .

spacecraft observations (e.g., Divin et al. 2015b; Cozzani et al. 2021). Moreover, PIC simulations found that other instabilities can also cause kinetic scale turbulences in reconnection, such as the Buneman instability (Drake et al. 2003), current filamentation instability (Che et al. 2011), interchange instability (e.g., Lapenta et al. 2015; Pucci et al. 2017), and electron Kelvin–Helmholtz instability (e.g., Huang et al. 2017; Che & Zank 2020). On the other hand, direct spacecraft observations showed that the turbulences in kinetic scale magnetic reconnection can be caused by magnetic holes (i.e., depletion in magnitude of magnetic field) and electrostatic and electromagnetic waves (Ergun et al. 2016, 2017, 2020).

The above spacecraft observations and numerical simulations show that the constitution of the turbulences in kinetic scale reconnection is diverse; therefore, in this paper, we adopt a turbulent forcing as a collective manifestation of the various instabilities, waves, and coherent structures, and we impose the turbulent forcing into two-dimensional PIC simulations to study kinetic scale turbulent magnetic reconnection. The simulation model is described in the following Section 2, the simulation results are presented in Section 3, and Section 4 is the conclusions and discussion.

2. Simulation Model

We use a PIC simulation model, and it is 2D in the x - z plane. The initial configuration is the Harris current sheet with magnetic field $\mathbf{B}(z) = B_0 \tanh(z/L)\mathbf{e}_x$ and plasma density $n(z) = n_b + n_0 \operatorname{sech}^2(z/L)$, where B_0 is magnitude of the asymptotic magnetic field, n_b is the background density, n_0 is the peak density in the Harris current sheet, and L is half-thickness of the current sheet. In our simulations, we use $n_b = 0.2n_0$ and $L = 0.5d_i$, where d_i is the ion inertial length evaluated using n_0 . The initial ion and electron temperatures are uniform, with $T_{i0} = 0.4m_iV_A^2$ and $T_{e0} = 0.1m_eV_A^2$, where m_i is

the ion mass and V_A is the Alfvén velocity evaluated using B_0 and n_0 .

The simulation domain $[-L_x/2, L_x/2] \times [-L_z/2, L_z/2]$ is discretized into grid cells, with $L_x = 204.8d_i$, $L_z = 51.2d_i$, and the grid size is $\Delta x = \Delta z = 0.05d_i$, corresponding to a grid number of $N_x \times N_z = 4096 \times 1024$. Electric field and magnetic field are defined on the grids and updated by solving Maxwell’s equations using an explicit algorithm. Ions and electrons are treated as full particles, and their positions and velocities are advanced by solving their equation of motion. The ion-to-electron mass ratio $m_i/m_e = 100$, and the speed of light $c = 20V_A$. The unit density n_0 is represented by 610 particles per species per grid cell. Periodic and perfect conductor boundary conditions are used in the x - and z -directions, respectively.

A small perturbation in magnetic field is added at $(x, z) = (0, 0)$ to expedite the onset of magnetic reconnection. Once reconnection begins, to evolve magnetic reconnection into a turbulent regime, we impose a turbulent forcing on the ions through the following procedure. We give a turbulent ion flow velocity $d\mathbf{V}$ with $dV_x = \sum_m \sum_n V_{mn} n \sin\left(\frac{2\pi m}{L_0}x + \phi_{mn}\right) \cos\left(\frac{2\pi n}{L_0}z + \psi_{mn}\right)$, $dV_y = 0$, and $dV_z = -\sum_m \sum_n V_{mn} m \cos\left(\frac{2\pi m}{L_0}x + \phi_{mn}\right) \sin\left(\frac{2\pi n}{L_0}z + \psi_{mn}\right)$. The turbulent forcing is therefore $\mathbf{F}_t = m_i d\mathbf{V}/dt$, where $dt = 0.001\Omega_i^{-1}$ is the time step, and $\Omega_i = eB_0/m_i$ is the ion gyrofrequency. Then we interpolate it to the position of each ion and obtain the turbulent forcing on each ion. Each mode $V_{mn} = dV_0/[(m^2 + n^2)(l_{\max}^2 - l_{\min}^2)]^{1/2}$, where $l_{\min} \leq (m^2 + n^2)^{1/2} \leq l_{\max}$, dV_0 determines the magnitude of the turbulent forcing, ϕ_{mn} and ψ_{mn} are random phases, and L_0 is the maximum spatial scale of the turbulent forcing. We set $L_0 = 51.2d_i$, $l_{\min} = 1$, and $l_{\max} = 8$, which gives the wavenumber k of the turbulent forcing, $0.1 < kd_i < 1$, i.e., the turbulent forcing is on ion scales, and this is why we impose it on ions and let it cascade to smaller-scale electrons self-consistently.

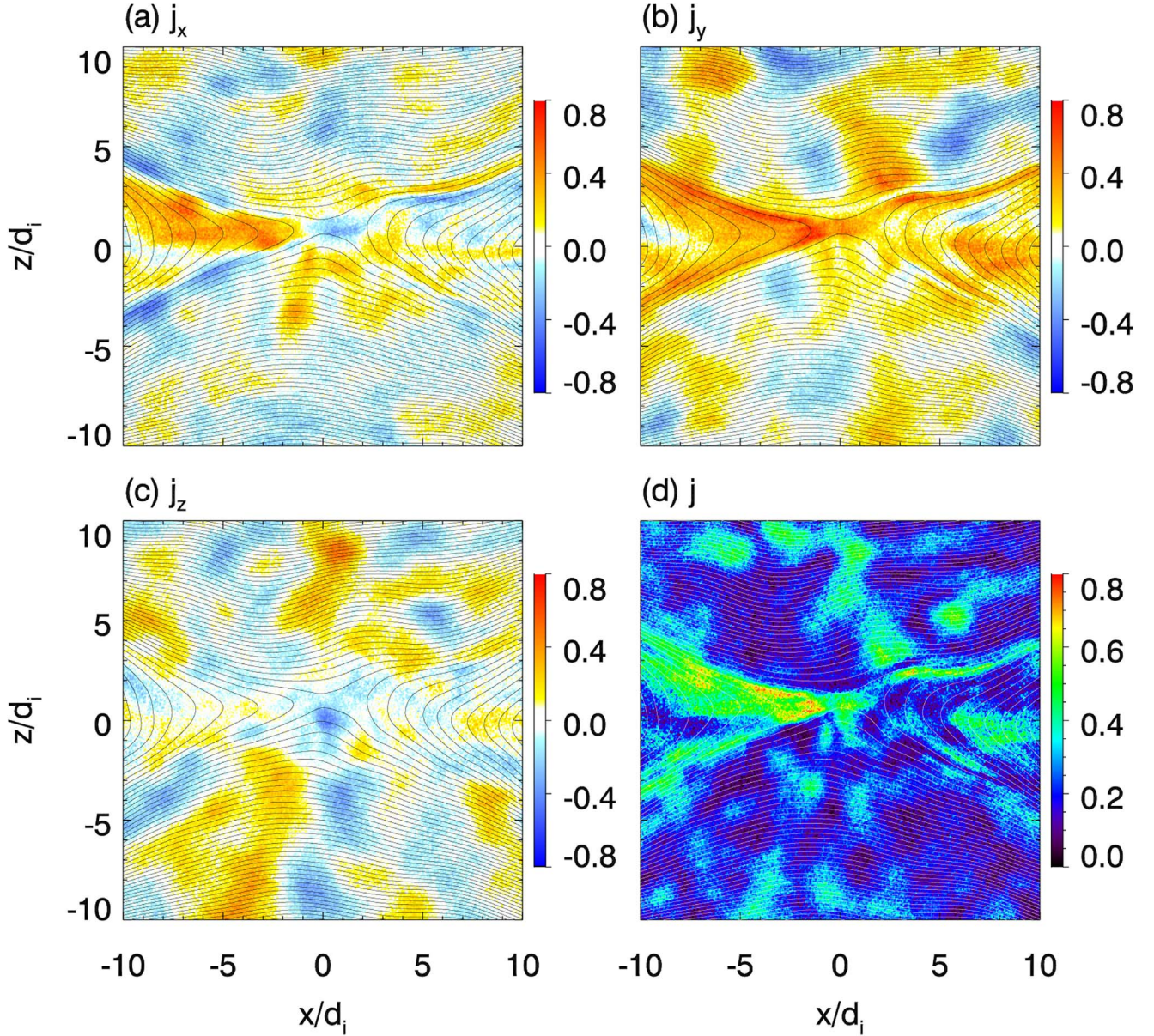


Figure 2. Zoomed-in view of current density (a) j_x , (b) j_y , (c) j_z , and (d) its magnitude j at $\Omega_i t = 70$ with $dV_0 = 0.03V_A$. The curves represent the in-plane magnetic field lines. The current density is in units of en_0V_A .

3. Simulation Results

Figure 1 shows a representative case with a turbulent forcing $dV_0 = 0.03V_A$ added after magnetic reconnection begins at $\Omega_i t = 30$. Because of the turbulent forcing, the magnetic field lines and the current density become fluctuated. Figure 2 shows the zoomed-in view of the current density at the fluctuating X-line at $\Omega_i t = 70$. The current density presents a filamentary pattern, and the current is in the x , y , z all three directions. The quadrupolar Hall magnetic field B_y and the bipolar Hall electric field E_x and E_z are typical in laminar reconnection ($dV_0 = 0$, see Figures 3(a), (c), and (e)); in the case with $dV_0 = 0.03V_A$, the Hall magnetic field persists but is interfered by the magnetic fluctuations (Figures 3b), whereas the Hall electric field is fully surpassed by the electric fluctuations (Figures 3(d) and (f)). The electric field in the out-of-plane direction E_y is also fluctuated with an amplitude of about $\sim 2V_A B_0$ (Figure 3(h)), much larger than the typical magnitude of the reconnection electric field,

$\sim 0.2V_A B_0$ (Figure 3(g)). The ion and electron outflows also become fluctuated but still retain the bidirectional patterns that are typical in laminar reconnection (Figures 3(i)–(l)). The energy conversion $\mathbf{j} \cdot \mathbf{E}$ is nonzero in the diffusion region and peaks at the reconnection fronts in laminar reconnection (Figure 3(m)), and $\mathbf{j} \cdot \mathbf{E}'$ (where $\mathbf{E}' = \mathbf{E} + \mathbf{v}_e \times \mathbf{B}$) is nonzero only in the vicinity of the X-line (i.e., electron diffusion region) in laminar reconnection (Figure 3(o)). In the case with $dV_0 = 0.03V_A$, both $\mathbf{j} \cdot \mathbf{E}$ and $\mathbf{j} \cdot \mathbf{E}'$ are nonzero not only at the X-line but also throughout the entire domain (Figures 3(n) and (p)). Therefore, although nonzero $\mathbf{j} \cdot \mathbf{E}'$ has been commonly used as a criterion for electron diffusion regions in laminar reconnection (e.g., Lu et al. 2022b), it should be used with caution in turbulent reconnection.

We show time histories of the reconnected magnetic flux and the reconnection rate in Figure 4. Although the out-of-plane electric field E_y is fluctuated with a large amplitude (Figure 3(h)) in the case with $dV_0 = 0.03V_A$, the reconnection

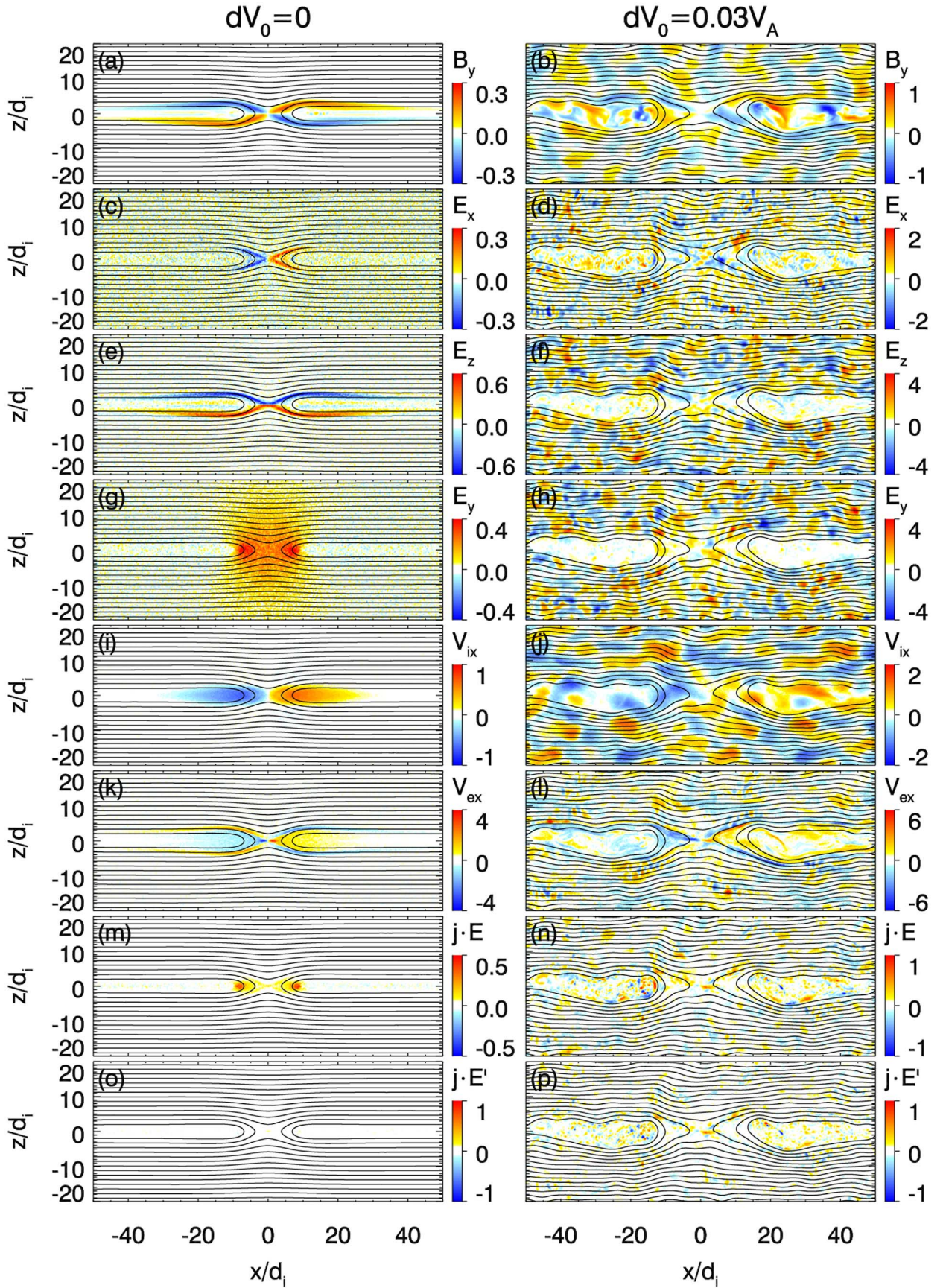


Figure 3. Contours of (a), (b) magnetic field B_y , (c), (d) electric field E_x , (e), (f) electric field E_z , (g), (h) electric field E_y , (i), (j) ion flow velocity V_{ix} , (k), (l) electron flow velocity V_{ex} , (m), (n) $\mathbf{j} \cdot \mathbf{E}$, and (o), (p) $\mathbf{j} \cdot \mathbf{E}'$ in the cases with $dV_0 = 0$ (left) and $dV_0 = 0.03V_A$ (right) at $\Omega_{ci}t = 50$. The curves represent the in-plane magnetic field lines. The magnetic field is in units of B_0 , the electric field is in units of $V_A B_0$, the flow velocity is in units of V_A , and $\mathbf{j} \cdot \mathbf{E}$ and $\mathbf{j} \cdot \mathbf{E}'$ are in units of $en_0 V_A^2 B_0$.

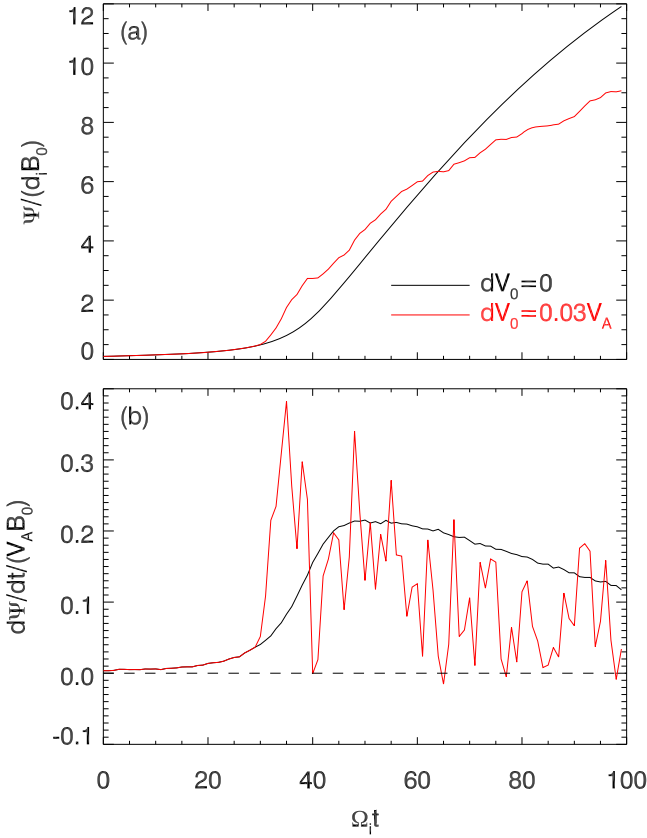


Figure 4. Time histories of (a) reconnected magnetic flux Ψ and (b) reconnection rate $d\Psi/dt$ in the cases with $dV_0 = 0$ (black) and $dV_0 = 0.03V_A$ (red). Here the reconnected magnetic flux is defined as the difference between the maximum and minimum vector potential A_y at $B_x = 0$. The reconnected magnetic flux is in units of dB_0 , the reconnection rate is in units of $V_A B_0$.

rate is still about $\sim 0.2V_A B_0$, similar to that in laminar reconnection with $dV_0 = 0$. The reconnected magnetic flux is also close in these two cases. This is different from MHD scale reconnection in which the turbulent forcing can dramatically increase the reconnection rate (e.g., Kowal et al. 2009; Loureiro et al. 2009; Kowal et al. 2012; Yang et al. 2020; Sun et al. 2022). The reconnection rate is decreased in the late phase because the electron diffusion region elongates (e.g., Daughton et al. 2006). Note that the turbulent forcing further decreases the reconnection rate. This may be because the turbulent forcing provides additional ion energization so that the high ion pressure in unreconnected regions can suppress magnetic reconnection.

Figure 5 shows virtual spacecraft observations at the X-line, $(x, z) = (0, 0)$. Right after the turbulent forcing is turned on at $\Omega_i t = 30$, the fluctuations emerge at the X-line. The three components of the magnetic field are fluctuated with $\delta B_x \approx 0.4B_0$ and $\delta B_y \approx \delta B_z \approx 0.2B_0$ (Figure 5(a)). The electric field fluctuations are strong, with a large magnitude of $\sim 2V_A B_0$ (Figure 5(c)), larger than that of the reconnection electric field (Figure 3(g)) and the Hall electric field (Figures 3(c) and (e)). The fluctuated magnetic field is self-consistent with the filamentary current that is fully fragmented with well-separated spikes in current density (Figure 5(e)). The filamentary current is mostly carried by the electrons in the y -direction, with the maximum $|V_{ey}| \approx 7V_A$, whereas the amplitude of V_{ex} and V_{ez} fluctuations is about $3V_A$ (Figure 5(d)), and the amplitude of V_i fluctuations $\approx V_A$ (Figure 5(b)). The virtual spacecraft

observations, which show more fine structures than in the snapshots (Figures 1–3), suggest that the observed filamentary currents and electromagnetic fluctuations originate from not only their spatial structures but also their temporal evolution.

The filamentary current density is well correlated with the spikes in $\mathbf{j} \cdot \mathbf{E}'$ (Figure 5(f)). The maximum $\mathbf{j} \cdot \mathbf{E}'$ is larger than $1.2en_0 V_A^2 B_0$, much larger than the typical value of about $0.2en_0 V_A^2 B_0$ in laminar reconnection (Figure 3(o)). Note that the work done by the Lorentz force $\mathbf{V} \cdot (\mathbf{j} \times \mathbf{B})$ is small, so $\mathbf{j} \cdot \mathbf{E} = \mathbf{V} \cdot (\mathbf{j} \times \mathbf{B}) + \mathbf{j} \cdot \mathbf{E}' \approx \mathbf{j} \cdot \mathbf{E}'$. The $\mathbf{j} \cdot \mathbf{E}'$ spikes are also well correlated with peaks in electron temperature (Figure 5(g)) and enhancements in electron energy distribution functions (Figure 5(h)). The electrons keep being heated and accelerated, as indicated by the temperature increase from $0.1m_i V_A^2$ to about $0.3m_i V_A^2$ (Figure 5(g)) and the energy increase in the tail of its distribution function with energy exceeds $1.0m_e c^2$ (Figure 5(h)).

Figure 6 shows the power spectra of the magnetic field and the electric field from the virtual spacecraft observations at the X-line. The magnetic field and electric field both follow a double power-law spectrum with a spectral break near $\omega \approx 3\Omega_i$. The local magnetic field is fluctuating with an average magnitude of $B^* \approx 0.22B_0$, so the local ion gyrofrequency $\Omega_i^* = 0.22\Omega_i$, the local electron gyrofrequency $\Omega_e^* = 22\Omega_i$, and the local lower-hybrid frequency $\omega_{LH}^* = 2.2\Omega_i$. Therefore, the spectral break is near the local lower-hybrid frequency. Between the local ion gyrofrequency and the local lower-hybrid frequency, the slope of the magnetic field power spectrum is about -1.99 , and that of the electric field is about -1.18 . Above the local lower-hybrid frequency, the magnetic field and the electric field have steeper spectra with slopes of about -4.41 and -2.91 , respectively. The power-law spectra and the spectral break are typical in plasma turbulence (e.g., Alexandrova et al. 2009). Therefore, kinetic scale magnetic reconnection with the turbulent forcing evolves into turbulent reconnection, with energy cascade from large to small scales and dissipation at local lower-hybrid frequency.

We have shown in Figure 5(h) that the electrons keep being accelerated at the X-line in turbulent reconnection with $dV_0 = 0.03V_A$. In Figure 7, we show the electron energy distribution for cases with different magnitudes of the turbulent forcing. In laminar reconnection with $dV_0 = 0$, the electrons are accelerated, and the high energy electrons form a soft power-law spectrum with a slope of -5.95 . In turbulent reconnection with $dV_0 = 0.03V_A$, the electron acceleration is more efficient in the high energy part, which also forms a harder power-law spectrum with a slope of -3.69 . When the turbulent forcing is increased to $dV_0 = 0.05V_A$, the electrons at the X-line are heated to higher energies, but the spectral slope of the energetic part remains -3.68 . To understand the electron acceleration mechanism, we plot the electron velocity distributions in Figure 8. In laminar reconnection ($dV_0 = 0$), the electrons are accelerated by the reconnection electric field when they follow the Speiser-type meandering motion at the X-line, as shown by the two positive and negative v_{ez} peaks (Figure 8(a)) and the negative v_{ey} peak (Figure 8(b)). In turbulent reconnection ($dV_0 = 0.03V_A$ and $dV_0 = 0.05V_A$), the high energy electrons are isotropic, suggesting a stochastic acceleration in the turbulent electric and magnetic fields (Zank et al. 2014; Che & Zank 2020).

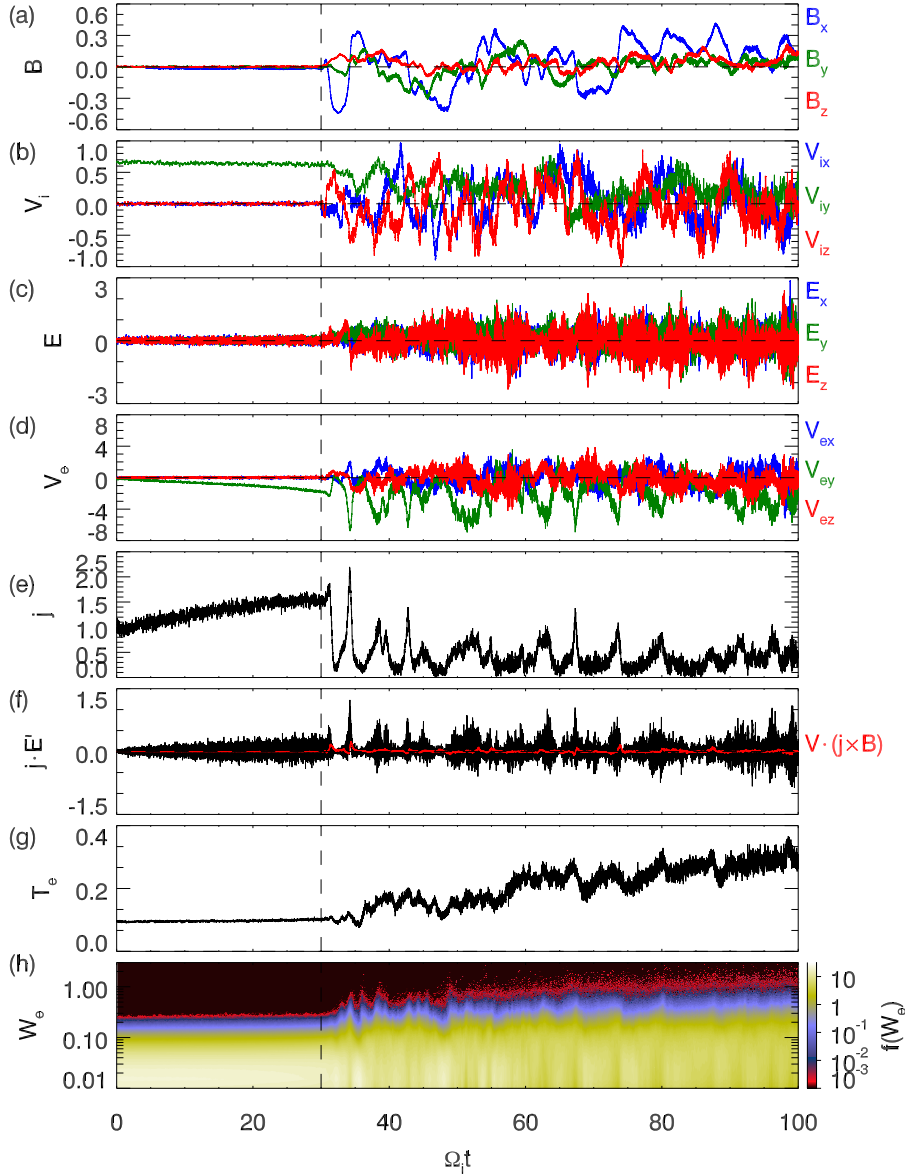


Figure 5. Virtual spacecraft observations at the X-line, $(x, z) = (0, 0)$ in the case with $dV_0 = 0.03V_A$. (a) Three components of magnetic field, (b) three components of ion flow velocity, (c) three components of electric field, (d) three components of electron flow velocity, (e) magnitude of current density, (f) energy conversion $\mathbf{j} \cdot \mathbf{E}'$ and work done by Lorentz force $\mathbf{V}_e \cdot (\mathbf{j} \times \mathbf{B}) = \mathbf{V}_i \cdot (\mathbf{j} \times \mathbf{B})$, (g) electron temperature, and (h) electron energy distribution function $f(W_e)$, where $\int f(W_e) dW_e = 1$. The vertical dashed line represents the time when the turbulent forcing is turned on. The magnetic field is in units of B_0 , the electric field is in units of $V_A B_0$, the flow velocity is in units of V_A , the energy conversion and the work done by Lorentz force are in units of $en_0 V_A^2 B_0$, the electron temperature is in units of $m_i V_A^2$, and the electron energy W_e is in units of $m_e c^2$.

4. Conclusions and Discussion

Our PIC simulations show that turbulent forcing can transform kinetic scale magnetic reconnection from laminar to turbulent. In the kinetic scale turbulent reconnection, the electric field and magnetic field become fluctuated, and filamentary current structures are formed. The fluctuated electric field and magnetic field at the X-line both exhibit a double power-law behavior with a spectral break near local lower-hybrid frequency. The electromagnetic turbulence barely changes the reconnection rate. The filamentary current has peaks in current density that are well correlated with spikes of energy conversion $\mathbf{j} \cdot \mathbf{E}'$. In general, $\mathbf{j} \cdot \mathbf{E}'$ is much larger in turbulent reconnection than laminar reconnection, leading to significant electron energization. At the X-line in turbulent reconnection, the electrons are accelerated to form a power-law

spectrum in the high energy tail, with a slope of about -3.7, much harder than that in laminar reconnection. The velocity distributions of the energetic electrons are isotropic in turbulent reconnection, suggesting a stochastic acceleration mechanism.

Although kinetic scale turbulent magnetic reconnection has been commonly observed in Earth's magnetotail, the observations were mostly in the ion diffusion region or the outflow region (e.g., Eastwood et al. 2009). Recently, Li et al. (2022b) reported Magnetospheric Multiscale (MMS) observations of the X-line region in turbulent reconnection, which presented filamentary currents, turbulent electric- and magnetic fields, and superthermal electrons. In Table 1, we compare the X-line properties obtained from our PIC simulations of laminar reconnection ($dV_0 = 0$) and turbulent reconnection ($dV_0 = 0.03V_A$) and the MMS observations of turbulent reconnection in Li et al. (2022b). It

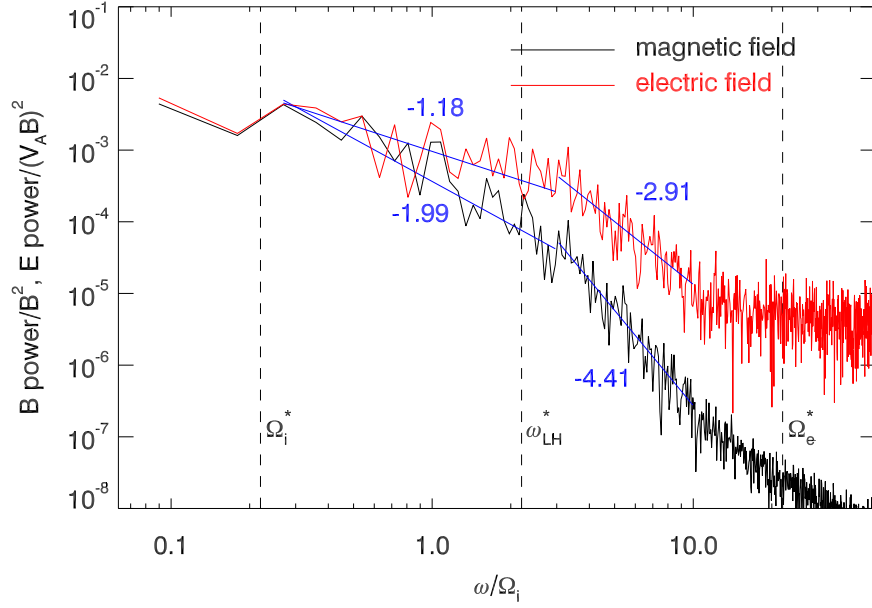


Figure 6. Power spectra of the magnetic field (black) and electric field (red) obtained from the virtual spacecraft observations at the X-line, $(x, z) = (0, 0)$, from $\Omega_i t = 30$ to $\Omega_i t = 100$ in the case with $dV_0 = 0.03V_A$. The magnetic field power is in units of B_0^2 , and the electric field power is in units of $(V_A B_0)^2$. Here frequency is in units of $\Omega_i = eB_0/m_i$. The three vertical dashed lines represent local ion gyrofrequency Ω_i^* , local lower-hybrid frequency ω_{LH}^* , and local electron gyrofrequency Ω_e^* . Because the magnetic field at $(x, z) = (0, 0)$ averaged from $\Omega_i t = 30$ to $\Omega_i t = 100$ is $B^* = 0.22B_0$, we have $\Omega_i^* = eB^*/m_i = 0.22\Omega_i$, $\omega_{LH}^* = 2.2\Omega_i$, and $\Omega_e^* = 22\Omega_i$.

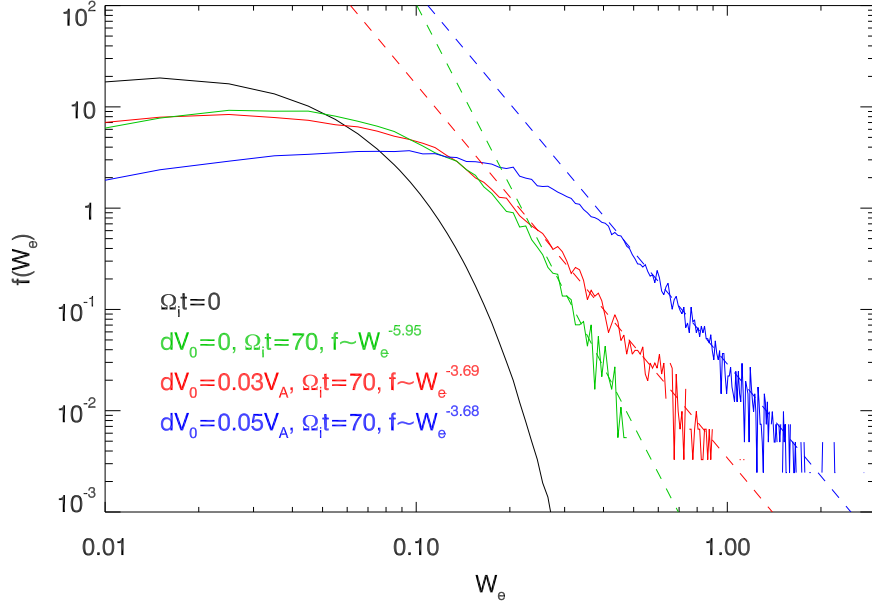


Figure 7. Electron energy distribution function $f(W_e)$ at the X-line, $(x, z) = (0, 0)$, at $\Omega_i t = 0$ (black), $\Omega_i t = 70$ with $dV_0 = 0$ (green), $\Omega_i t = 70$ with $dV_0 = 0.03V_A$ (red), and $\Omega_i t = 70$ with $dV_0 = 0.05V_A$ (blue). Here $\int f(W_e) dW_e = 1$, and the electron energy W_e is in units of $m_e c^2$.

is clear that the filamentary currents, the strong electromagnetic fluctuations, and the double power-law spectral behavior with a break at local lower-hybrid frequency in the MMS observations are well reproduced in our PIC simulations by imposing a turbulent forcing on ions. Nevertheless, there are some quantitative differences between the observations and simulations, for example, the energetic electron power-law index in the MMS observations is about 8.0, whereas our simulations give a much harder power-law index of about 3.7.

Our simulations show that electron acceleration at the X-line is more efficient in turbulent reconnection than laminar reconnection. In laminar reconnection, the electrons follow a Speiser-type meandering motion at the X-line and are

accelerated in the meantime by the reconnection electric field (e.g., Fu et al. 2006; Ng et al. 2011). However, the X-line configuration in laminar reconnection cannot well confine the electrons because the electrons can escape from the X-line in the x -direction. Therefore, the acceleration is not sufficient enough to produce hard power-law spectra for the electrons, and indeed, our simulations give a soft power-law index of ~ 6 at the X-line in laminar reconnection. For turbulent reconnection, the electron energy spectrum is much harder, with a power-law index of ~ 3.7 , which may be because the electrons are trapped at the X-line for a longer time in turbulent reconnection (Matthaeus et al. 1984), and this type of electron acceleration in the stochastic electromagnetic fields can be well

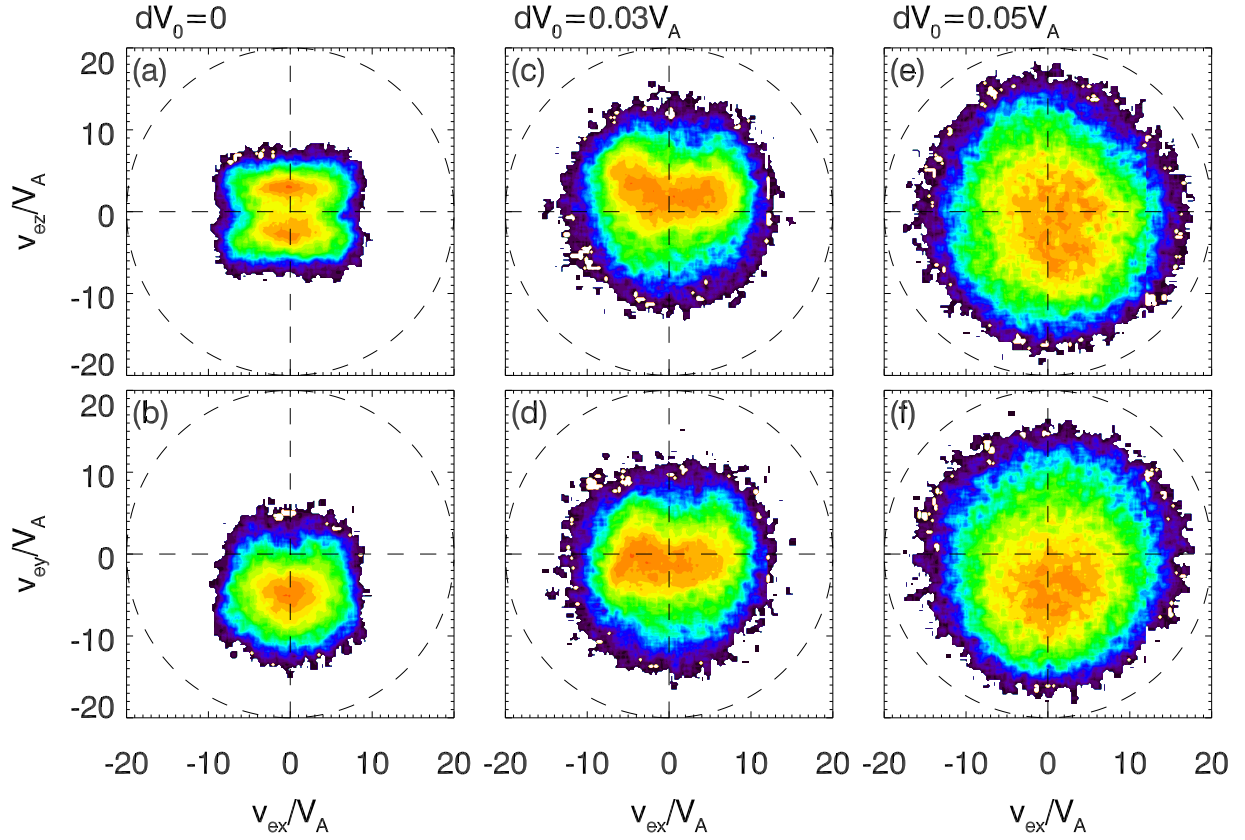


Figure 8. Electron velocity distribution functions $f(v_{ex}, v_{ez})$ (top) and $f(v_{ex}, v_{ey})$ (bottom) at the X-line, $(x, z) = (0, 0)$, at $\Omega_e t = 70$ in the cases with different magnitudes of the turbulent forcing $dV_0 = 0$ (left), $dV_0 = 0.03V_A$ (middle), and $dV_0 = 0.05V_A$ (right). The electron particle velocity is in units of V_A . The velocity distribution functions are displayed using a logarithm scale.

Table 1

Properties of the Reconnection X-line Obtained from PIC Simulations of Laminar Reconnection ($dV_0 = 0$) and Turbulent Reconnection ($dV_0 = 0.03V_A$) and MMS Observations of Turbulent Reconnection in Li et al. (2022b)

	PIC Simulations of Laminar Reconnection ($dV_0 = 0$)	PIC Simulations of Turbulent Reconnection ($dV_0 = 0.03V_A$)	MMS Observations of Turbulent Reconnection (Li et al. 2022b)
Filamentary currents	No	Yes	Yes
Maximum $\mathbf{j} \cdot \mathbf{E}'$ in units of $en_0 V_A^2 B_0$	0.54	1.23	1.12
Average $ \mathbf{B} $ in units of B_0	0.011	0.22	0.37
Maximum $(\delta B_x, \delta B_y, \delta B_z)$ in units of B_0	(0.020, 0.019, 0.016)	(0.37, 0.26, 0.18)	(0.39, 0.43, 0.48)
Average $ \mathbf{E} $ in units of $V_A B_0$	0.28	0.79	0.99
Maximum $(\delta E_x, \delta E_y, \delta E_z)$ in units of $V_A B_0$	(0.37, 0.40, 0.70)	(2.86, 2.30, 2.45)	(0.96, 1.48, 2.88)
Power-law spectral break at ω_{LH}^*	No	Yes	Yes
Magnetic field spectral indices	...	1.99 (above ω_{LH}^*) 4.41 (below ω_{LH}^*)	2.31 (above ω_{LH}^*) 3.3 (below ω_{LH}^*)
Electric field spectral indices	...	1.18 (above ω_{LH}^*) 2.91 (below ω_{LH}^*)	1.26 (above ω_{LH}^*) 2.96 (below ω_{LH}^*)
Reconnection rate	~ 0.2	~ 0.2	...
Energetic electron power-law index	6.0	3.7	8.0
Peak in electron temperature in units of $m_i V_A^2$	0.19	0.37	0.31

Note. Here ω_{LH}^* is the average local lower-hybrid frequency. From the MMS observations, the maximum $\mathbf{j} \cdot \mathbf{E}$, is 1.31 nW m⁻¹, the average $|\mathbf{B}|$ is 9.33 nT, the maximum $(\delta B_x, \delta B_y, \delta B_z)$ is (9.78, 10.73, 11.92) nT, the average $|\mathbf{E}|$ is 42.2 mV m⁻¹, the maximum $(\delta E_x, \delta E_y, \delta E_z)$ is (40.6, 62.9, 122.2) mV m⁻¹, and the peak in electron temperature is 9.3 keV. To compare with the simulation results, the observation results are normalized to simulation units using the observed parameters, $B_0 = 25$ nT and $n_0 = 0.1$ cm⁻³.

explained by the second-order Fermi acceleration mechanism (Zank et al. 2014; Che & Zank 2020). However, it requires further examination to understand quantitatively why the power-law index is ~ 3.7 in the turbulent reconnection with $dV_0 = 0.03V_A$ and why the index does not change with a stronger turbulent forcing $dV_0 = 0.05V_A$.

Previous PIC simulation results have suggested various self-consistent instabilities, waves, and coherent structures to form turbulences in kinetic scale turbulent reconnection (see Section 1). Here, from a different perspective, we launch kinetic scale turbulent reconnection by imposing a turbulent forcing as a collective manifestation to imitate the effect of

these instabilities, waves, or coherent structures. Although turbulent forcing has been commonly used to launch MHD scale turbulent reconnection (e.g., Kowal et al. 2009, 2012; Loureiro et al. 2009; Sun et al. 2022), here it is used for the first time to launch kinetic scale turbulent reconnection. By imposing a turbulent forcing on the ions, although our simulations (as shown in Table 1) can well reproduce the X-line characteristics in the MMS observations reported by Li et al. (2022b), the effects of other forms of turbulent forcing on kinetic scale magnetic reconnection require further investigation. Moreover, our present simulations are 2D, it is important to study 3D effects of the turbulent forcing on kinetic scale reconnection in future work.

This work was supported by National Natural Science Foundation of China (NSFC) grants 42274196 and 42174181, Strategic Priority Research Program of Chinese Academy of Sciences grant XDB41000000, and ISSI-BJ International Team “Interaction between magnetic reconnection and turbulence: From the Sun to the Earth.” Computer resources were provided by Beijing Super Cloud Computing Center.

ORCID iDs

San Lu  <https://orcid.org/0000-0003-2248-5072>
 Quanming Lu  <https://orcid.org/0000-0003-3041-2682>
 Rongsheng Wang  <https://orcid.org/0000-0002-9511-7660>
 Xinmin Li  <https://orcid.org/0000-0003-1553-6337>
 Xinliang Gao  <https://orcid.org/0000-0003-0767-2267>
 Kai Huang  <https://orcid.org/0000-0003-3630-309X>
 Haomin Sun  <https://orcid.org/0000-0001-7403-6450>
 Yan Yang  <https://orcid.org/0000-0003-2965-7906>
 Anton V. Artemyev  <https://orcid.org/0000-0001-8823-4474>
 Xin An  <https://orcid.org/0000-0003-2507-8632>
 Yingdong Jia  <https://orcid.org/0000-0002-1631-291X>

References

- Alexandrova, O., Saur, J., Lacombe, C., et al. 2009, *PhRvL*, **103**, 165003
 Bhattacharjee, A., Huang, Y.-M., Yang, H., & Rogers, B. 2009, *Phys Plasmas*, **16**, 112102
 Borg, A. L., Øieroset, M., Phan, T. D., et al. 2005, *GeoRL*, **32**, L19105
 Burch, J. L., Torbert, R. B., Phan, T. D., et al. 2016, *Sci*, **352**, aaf2939
 Che, H., Drake, J. F., & Swisdak, M. 2011, *Natur*, **474**, 184
 Che, H., & Zank, G. P. 2020, *ApJ*, **889**, 11
 Cheng, X., Li, Y., Wan, L. F., et al. 2018, *ApJ*, **866**, 64
 Cozzani, G., Khotyaintsev, Y., Graham, D. B., et al. 2021, *PhRvL*, **127**, 215101
 Daughton, W., Roytershteyn, V., Karimabadi, H., et al. 2011, *NatPh*, **7**, 539
 Daughton, W., Scudder, J., & Karimabadi, H. 2006, *Phys Plasmas*, **13**, 072101
 Divin, A., Khotyaintsev, Y. V., Vaivads, A., et al. 2015a, *JGRA*, **120**, 2675
 Divin, A., Khotyaintsev, Y. V., Vaivads, A., & Andre, M. 2015b, *JGRA*, **120**, 1124
 Drake, J. F., Swisdak, M., Cattell, C., et al. 2003, *Sci*, **299**, 873
 Eastwood, J. P., Phan, T. D., Bale, S. D., & Tjulin, A. 2009, *PhRvL*, **102**, 035001
 Eastwood, J. P., Phan, T. D., Øieroset, M., & Shay, M. A. 2010, *JGRA*, **115**, A08215
 Ergun, R. E., Ahmadi, N., Kromyda, L., et al. 2020, *ApJ*, **898**, 154
 Ergun, R. E., Chen, L.-J., Wilder, F. D., et al. 2017, *GeoRL*, **44**, 2978
 Ergun, R. E., Holmes, J. C., Goodrich, K. A., et al. 2016, *GeoRL*, **43**, 5626
 Ergun, R. E., Pathak, N., Usanova, M. E., et al. 2022, *ApJL*, **935**, L8
 Fu, H. S., Vaivads, A., Khotyaintsev, Y. V., et al. 2017, *GeoRL*, **44**, 37
 Fu, X. R., Lu, Q. M., & Wang, S. 2006, *PhPl*, **13**, 012309
 Gosling, J. T., Skoug, R. M., McComas, D. J., & Smith, C. W. 2005, *JGRA*, **110**, A01107
 Huang, C., Lu, Q., Wang, R., et al. 2017, *ApJ*, **835**, 245
 Huang, S. Y., Zhou, M., Sahraoui, F., et al. 2012, *GeoRL*, **39**, L11104
 Jin, R., Zhou, M., Pang, Y., Deng, X., & Yi, Y. 2022, *ApJ*, **925**, 17
 Kowal, G., Lazarian, A., Vishniac, E. T., & Otmianowska-Mazur, K. 2009, *ApJ*, **700**, 63
 Kowal, G., Lazarian, A., Vishniac, E. T., & Otmianowska-Mazur, K. 2012, *NPGeo*, **19**, 297
 Lapenta, G., Markidis, S., Goldman, M. V., & Newman, D. L. 2015, *NatPh*, **11**, 690
 Lazarian, A., & Vishniac, E. T. 1999, *ApJ*, **517**, 700
 Li, X. M., Wang, R. S., Huang, C., et al. 2022a, *ApJ*, **936**, 34
 Li, X. M., Wang, R. S., Lu, Q. M., et al. 2022b, *NatCo*, **13**, 3241
 Loureiro, N. F., Schekochihin, A. A., & Cowley, S. C. 2007, *PhPl*, **14**, 100703
 Loureiro, N. F., Uzdensky, D. A., Schekochihin, A. A., Cowley, S. C., & Yousef, T. A. 2009, *MNRAS*, **399**, L146
 Lu, Q. M., Fu, H. S., Wang, R. S., & Lu, S. 2022a, *ChPhB*, **31**, 089401
 Lu, Q. M., Huang, C., Xie, J. L., et al. 2010, *JGRA*, **115**, A11208
 Lu, S., Angelopoulos, V., Artemyev, A. V., et al. 2019, *ApJ*, **878**, 109
 Lu, S., Artemyev, A. V., Angelopoulos, V., & Pritchett, P. L. 2020, *ApJ*, **896**, 105
 Lu, S., Lu, Q. M., Wang, R. S., et al. 2022b, *GeoRL*, **49**, e2022GL098547
 Masuda, S., Kosugi, T., Hara, H., Tsuneta, S., & Ogawara, Y. 1994, *Natur*, **371**, 495
 Matthaeus, W. H., Ambrosiano, J. J., & Goldstein, M. L. 1984, *PhRvL*, **53**, 1449
 Nagai, T., Shinohara, I., Fujimoto, M., et al. 2001, *JGRA*, **106**, 25929
 Ng, J., Egedal, J., Le, A., Daughton, W., & Chen, L.-J. 2011, *PhRvL*, **106**, 065002
 Øieroset, M., Phan, T. D., Fujimoto, M., Lin, R. P., & Lepping, R. P. 2001, *Natur*, **412**, 414
 Osman, K. T., Kiyani, K. H., Matthaeus, W. H., et al. 2015, *ApJL*, **815**, L24
 Parker, E. N. 1957, *JGR*, **62**, 509
 Phan, T. D., Gosling, J. T., Davis, M. S., et al. 2006, *Natur*, **439**, 175
 Phan, T. D., Lavraud, B., Halekas, J. S., et al. 2021, *A&A*, **650**, A13
 Price, L., Swisdak, M., Drake, J. F., et al. 2016, *GeoRL*, **43**, 6020
 Price, L., Swisdak, M., Drake, J. F., et al. 2017, *JGRA*, **122**, 11086
 Pritchett, P. L. 2001, *JGRA*, **106**, 3783
 Pucci, F., Servidio, S., Sorriso-Valvo, L., et al. 2017, *ApJ*, **841**, 60
 Pucci, F., & Velli, M. 2014, *ApJL*, **780**, L19
 Somov, B. V., & Kosugi, T. 1997, *ApJ*, **485**, 859
 Su, Y., Veronig, A. M., Holman, G. D., et al. 2013, *NatPh*, **9**, 489
 Sun, H., Yang, Y., Lu, Q., et al. 2022, *ApJ*, **926**, 97
 Sweet, P. A. 1958, in IAU Symp. 6, Electromagnetic Phenomena in Cosmical Physics, ed. B. Lehnert (Cambridge: Cambridge Univ. Press), 123
 Torbert, R. B., Burch, J. L., Phan, T. D., et al. 2018, *Sci*, **362**, 1391
 Tsuneta, S. 1996, *ApJ*, **456**, 840
 Vörös, Z., Sasunov, Y. L., Semenov, V. S., et al. 2014, *ApJL*, **797**, L10
 Wang, R., Lu, Q., Nakamura, R., et al. 2016, *NatPh*, **12**, 263
 Wang, R., Nakamura, R., Lu, Q., et al. 2017, *PhRvL*, **118**, 175101
 Wang, R. S., Wang, S. M., Lu, Q. M., et al. 2022, *NatAs*, in press
 Yamada, M., Kulsrud, R., & Ji, H. 2010, *RvMP*, **82**, 603
 Yang, L., Li, H., Guo, F., et al. 2020, *ApJL*, **901**, L22
 Zank, G. P., le Roux, J. A., Webb, G. M., Dosch, A., & Khabarova, O. 2014, *ApJ*, **797**, 28
 Zhou, M., Man, H. Y., Deng, X. H., et al. 2021, *GeoRL*, **48**, e2020GL091215